Badger, M. P. S., Lear, C. H., Pancost, R. D., Foster, G. L., Bailey, T., Leng, M. J., & Abels, H. (2013). CO_2 drawdown following the middle Miocene expansion of the Antarctic Ice Sheet. *Paleoceanography*, *28*(1), 42-53. https://doi.org/10.1002/palo.20015

CO_2 drawdown following the middle Miocene expansion of the Antarctic Ice Sheet.

Marcus P.S. Badger[1,2,3*], Caroline H. Lear[1], Richard D. Pancost[2], Gavin L. Foster[4], Trevor R. Bailey[5], Melanie J. Leng[6] & Hemmo A. Abels[7]

[1]*School of Earth and Ocean Sciences, Cardiff University, Main Building, Park Place, Cardiff, CF10 3YE, UK. *marcus.badger@bristol.ac.uk*

[2]*Organic Geochemistry Unit, The Cabot institute and Bristol Biogeochemistry Research Centre, School of Chemistry, University of Bristol, Cantock's Close, Bristol, BS8 1TS, UK.*

[3]*now at: School of Earth Sciences, Bristol University, Wills Memorial Building, Queens Rd, Bristol, BS8 1RJ, UK.*

[4]*Bristol Isotope Group, School of Earth Sciences, Bristol University, Wills Memorial Building, Queens Rd, Bristol, BS8 1RJ, UK. Now at: Ocean and Earth Science, National Oceanography Centre Southampton, University of Southampton Waterfront Campus, Southampton, SO14 3ZH, UK.*

[5]*Geology Department, Amgueddfa Cymru-National Museum Wales, Cathays Park, Cardiff, CF10 3NP, UK.*

[6]*Department of Geology, University of Leicester, Leicester, LE1 7RH, UK and NERC Isotope Geosciences Laboratory, British Geological Survey, Nottingham NG12 5GG, UK.*

[7]*Stratigraphy / Paleontology, Dept.of Earth Sciences, University of Utrecht, 3584 CD, Utrecht, The Netherlands.*

The development of a permanent, stable ice sheet in East Antarctica happened during the middle Miocene, about 14 Myr (million years) ago. The middle Miocene therefore represents one of the distinct phases of rapid change in the transition from the "greenhouse" of the early Eocene to the "icehouse" of the present day. Carbonate carbon isotope records of the period immediately following the main stage of ice sheet development reveal a major perturbation in the carbon system, represented by the positive $\delta^{13}C$ excursion known as carbon maximum 6 ("CM6"), which has traditionally been interpreted as reflecting increased burial of organic matter and atmospheric pCO_2 drawdown. More recently, it has been suggested that the $\delta^{13}C$ excursion records a negative feedback resulting from the reduction of silicate weathering and an increase in atmospheric pCO_2. Here we present high-resolution multi-proxy (alkenone carbon and foraminiferal boron isotope) records of atmospheric carbon dioxide and sea surface temperature across CM6. Similar to previously published records spanning this interval, our records document a world of generally low (~300 ppm) atmospheric pCO_2 at a time generally accepted to be much warmer than today. Crucially, they also reveal a pCO_2 decrease with associated cooling, which demonstrates that the carbon burial hypothesis for CM6 is feasible and could have acted as a positive feedback on global cooling.

1. Introduction

Accompanying the middle Miocene growth of the East Antarctic Ice Sheet (EAIS) are major perturbations in the global carbon system, represented by some of the largest fluctuations in marine carbonate $\delta^{13}C$ values in the Cenozoic [*Flower and Kennett*, 1995; *Zachos et al.*, 2001]. A broad positive carbon isotope excursion (the "Monterey Excursion" [*Vincent and Berger*, 1985]) begins in the early Miocene (approximately 16.9 Myr ago) and terminates in the middle Miocene (~13.6 Myr ago [*Holbourn et al.*, 2007]). Within this broad $\delta^{13}C$ excursion, higher frequency fluctuations have been recognised with at least seven carbon isotope maxima (CM) defined

[*Woodruff and Savin,* 1991]. These positive carbon isotope excursions are traditionally interpreted as the result of increased burial of organic carbon leading to a drawdown of carbon dioxide from the atmosphere, and subsequent global cooling and ice build-up [*Flower and Kennett,* 1993a; *Vincent and Berger,* 1985]. The largest of the carbon isotope maxima ("CM6" [*Woodruff and Savin,* 1991]) immediately follows the major ice expansion event of the middle Miocene ("E3"; [*Flower and Kennett,* 1993b] or "Mi-3"; [*Miller et al.,* 1991]) and therefore may represent an important positive feedback in the climate system.

However, it has recently been suggested that carbonate carbon isotope maxima associated with glacial transitions may be evidence of a negative feedback in the climate system [*Shevenell et al.,* 2008]. Under this alternative scenario, ice sheet expansion blankets an area of silicate basement that was previously a sink for atmospheric pCO_2 via silicate weathering [*Pagani et al.,* 1999; *Lear et al.,* 2004; *Shevenell et al.,* 2008*; Tian et al.,* 2009]. Both scenarios could result in positive carbonate carbon isotope excursions: the former by removal of ^{13}C-depleted carbon from the ocean-atmosphere reservoir as more organic matter is buried, and the latter by lowering buried organic matter $\delta^{13}C$ values as a result of increased photosynthetic isotopic fractionation (ε_p) due to higher concentrations of dissolved carbon dioxide ($[CO_{2(aq)}]$). Critically, these scenarios involve opposite changes in atmospheric carbon dioxide concentration. Therefore, to assess the likelihood of these mechanisms, we reconstruct atmospheric pCO_2 following the middle Miocene ice sheet expansion using two independent proxies: alkenone and boron isotope paleobarometry.

2. Materials and methods

The Blue Clay Formation of Malta (at Ras il-Pellegrin (RIP); Figure 1; 35°54.93'N 14°20.06'E) is a continuous land-based section of Miocene pelagic clays and marls with high sedimentation rates (40 $mMyr^{-1}$) [*Abels et al.,* 2005] and estimated paleo water depth of 500 to 600 m [*Bellanca et al., 2002; Bonaduce and Barra, 2002*]. The high clay content of the Blue Clay

Fm has resulted in excellent preservation of microfossils, and the simple tectonic history of Malta [*Dart et al.,* 1993] has resulted in material that has never been exposed to high temperatures or pressures, suggesting that primary geochemical signals should be preserved. The transition to the Blue Clay Formation from the older Globigerina Limestone Formation below coincides with the ice volume build-up "E3" [*Abels et al.*, 2005; *Woodruff and Savin,* 1991]. The associated change in preservation style precludes a continuous record across the entire climate transition. Nevertheless, we sampled the Blue Clay Formation at 35 cm (~9 kyrs) resolution enabling us to generate a stratigraphy of the 1.1 million years following ice volume build-up "E3". In the field, samples were tied to the lithostratigraphic log of *Abels et al.,* [2005]. Subsequent refinement was achieved by matching bulk isotope stratigraphies. The astronomical recalibration of the lower part of the Blue Clay Formation according to *Mourik et al.,* [2011] was used for the age model.

We analysed bulk and fine fraction (<63 μm) carbonate for δ^{13}C and δ^{18}O, and the planktic foraminifera *Globigerinoides trilobus* for Mg/Ca, δ^{13}C, δ^{18}O, B/Ca, and δ^{11}B. We also generated a compound specific (C_{37} alkenone) carbon isotope record.

2.1 Carbonate stable isotope stratigraphy

Bulk sediment and foraminiferal isotope analyses were performed on a ThermoFinnigan MAT252 with online sample preparation using an automated Kiel III carbonate device at Cardiff University. Long term uncertainties based on repeat analysis of NBS-19 are ±0.08 ‰ and ±0.05 ‰ for δ^{18}O and δ^{13}C respectively (2σ). Fine fraction isotope samples (<63 μm) were prepared offline and resultant CO_2 analysed using a VG Optima dual inlet gas source mass spectrometer at the NERC Isotope Geosciences Laboratory, analytical uncertainties are typically ±0.2 ‰ for both δ^{18}O and δ^{13}C (2σ). All isotope data are reported as per mil on the VPDB scale.

2.2 Planktic foraminiferal Mg/Ca analyses

Between 19 and 30 individuals of *G. trilobus* were picked from the 250-355 *μ*m size fraction and cleaned following the procedure of *Barker et al.* [2003]. In the modern ocean, *G. trilobus* is considered to be the same biological species as *G. sacculifer*, although *G. sacculifer* apparently did not evolve until the Pliocene [*Hemleben et al.,* 1989]. Here we assume *G. trilobus* and *G. sacculifer* are the same species. Samples were dissolved in 0.065 M nitric acid and analysed by sector field inductively coupled plasma mass spectrometry Thermo Scientific ELEMENT-XR (ICP-MS) at Cardiff University. Each sample was calibrated against a standard with matched Ca concentration to reduce matrix effects. Long-term analytical precision is better than 2 % (r.s.d.).

2.3 Organic geochemistry

5 g powdered samples were saponified and ultrasonically extracted using sequentially, methanoic 0.1 M KOH (5 % H_2O), methanol and a 3:1 (v/v) azeotrope of dichloromethane (DCM):methanol. Neutral fractions were obtained from the total extract by liquid-liquid separation with *n*-hexane:DCM (9:1 v/v) and silica gel column chromatography was used to divide samples into four fractions (F), eluted sequentially with *n*-hexane (4 ml, Fraction 1), *n*-hexane:DCM (2:1 v/v; 2 ml, F2), DCM (5 ml, F3) and DCM:Methanol (95:5 v/v; 5 ml, F4). Alkenones elute in F3, and their quantification for $U^{K'}_{37}$ calculation was performed on a Carlo Erba Instruments HRGC5300 gas chromatogram fitted with a flame ionisation detector and a Chrompack fused silica capillary column (50 m × 0.32 mm internal diameter; CP Sil-5CB stationary phase, dimethylpolysiloxane equivalent, 0.12 μm film thickness). Compound specific carbon isotope analyses were performed on a Finnigan MAT Delta S coupled to a GC with on-

column injector using a modified Finnigan MAT Type 1 GC combustion interface at the University of Bristol. A Zebron ZB-1 fused silica capillary column (50 m × 0.32 mm internal diameter; dimethylpolysiloxane equivalent stationary phase, 0.12 μm film thickness) was used. Samples were injected at 70 °C, and the oven programmed to increase in temperature to 130 °C at 20 °Cmin^{-1} then to 300 °C at 4 °Cmin^{-1}, remaining isothermal at 300 °C for 25 minutes. Long term uncertainties, on the basis of repeat standard measurements, are ±0.6 ‰ (2σ).

2.4 Foraminiferal δ^{11}B and B/Ca analyses

Six samples of *G. trilobus* (250-355 μm) each consisting of around 100 tests (~2 mg of $CaCO_3$) were analysed for boron isotopic composition on a ThermoFinnigan NEPTUNE multicollector ICP-MS at the University of Bristol following the methodology described by *Foster* [2008]. Analytical precision of this approach is ± 0.23 ‰ at 95 % confidence as determined by the long term reproducibility of full procedural replicates of an in house coral standard. Prior to isotope analysis, but following cleaning and dissolution, an aliquot of each sample was analysed for trace element content using a sector field ThermoFinnigan ELEMENT 2 ICP-MS [*Foster*, 2008; *Ni et al.*, 2007] at the University of Bristol. This analysis ensured cleaning was successful and provided a measure of B/Ca ratio for each sample. The long-term reproducibility of our in house consistency standards for B/Ca is ± 2 % (95% confidence) and our accuracy is better than 5 % [*Ni et al.*, 2007].

2.5 Mg/Ca paleotemperature equation

Critical to the accuracy of the alkenone and, to a lesser extent, the boron pCO_2 reconstruction is an accurate record of sea surface temperature (SST). However, foraminiferal calcite Mg/Ca is controlled not only by temperature, but also the Mg/Ca ratio of the seawater in which they calcify. The application of this proxy beyond the oceanic residence time of Ca and Mg (1 and 22 Myrs respectively; *Fantle and DePaolo, [2005; 2006]*) can therefore be complicated by changes in seawater Mg/Ca ratios (Mg/Ca_{sw}) with time. This is often corrected for by assuming a linear relationship between seawater Mg/Ca and foraminiferal Mg/Ca (e.g., *Lear et al.,* 2000) although it has been suggested that this dependency may be better described using a power function [*Hasiuk and Lohmann,* 2010] (equation 1).

$$(Mg/Ca)_{foram}=(Mg/Ca_{sw(t)}/Mg/Ca_{sw(0)})^{C}.Be^{AT} \quad (1)$$

Where $Mg/Ca_{foram,}$is the Mg/Ca ratio of foraminiferal calcite, $Mg/Ca_{sw(0)}$ and $Mg/Ca_{sw(t)}$ are the Mg/Ca ratios of seawater today and at time t respectively, A, B, and C are constants ('exponential', 'pre-exponential' and 'power' respectively) and T is temperature.

Mg and Ca are both delivered to the oceans via rivers and removed into sediments including carbonates. Hydrothermal alteration of basalt at ocean ridge systems represents an important sink for magnesium and source for calcium. All of these fluxes have varied over time. The residence times of Ca and Mg mean that Mg/Ca_{sw} is unlikely to have varied significantly over the duration of our record, but may have been considerably different in the Miocene compared to the present day. Attempts have been made to reconstruct Mg/Ca_{sw} over time using geochemical models [*Hardie,* 1996*; Wilkinson and Algeo,* 1989*, Fantle and DePaolo,* 2005; 2006], echinoderm skeletons [*Dickson,* 2002, 2004], fluid inclusions in marine evaporites [*Lowenstein et al., 2001, Horita et al.,* 2002] and carbonate veins precipitated in oceanic basalt [*Coggon et al.,* 2010]. Although these various reconstructions agree that Mg/Ca_{sw} was lower during the Miocene than today, its precise value remains unclear.

Here we apply the fluid inclusion based Mg/Ca_{sw} value of *Horita et al.,* [2002] (Mg/Ca_{sw}=3.43) to the generic planktic Mg/Ca paleotemperature equation of *Anand et al.,* [2003] (A=0.09, B=0.38 in equation 1), and apply the power constant for *G. sacculifer* (C=0.41 in equation 1) as determined by *Evans and Müller* [2012] based on the data of *Delaney et al.* [1985]. This results in the Mg/Ca_{sw} corrected paleotemperature equation given in equation 2.

$$Mg/Ca_{foram} = 0.32e^{0.09T} \quad (2)$$

The fluid inclusion data has the advantage over other methods of also providing absolute values for [Mg] and [Ca], as required to reconstruct carbonic acid dissociation constants K_1 and K_2 (see section 2.7).

2.6 Alkenone paleobarometry

Isotopic fractionation between dissolved inorganic carbon (DIC) and algal biomass (ε_p) occurs during photosynthesis and is strongly controlled by [$CO_{2(aq)}$] [*Laws et al.,* 1995], a relationship that serves as the basis of the phytoplankton-based pCO_2 paleobarometer [*Hollander and McKenzie,* 1991; *Pagani et al.,* 1999]. However, a range of other factors, including algal growth rate and cell geometry also govern ε_p values [*Bidigare et al.,* 1997; *Popp et al.,* 1998b]. In order to control source organism and restrict cell size effects, we measure the carbon isotopic composition of C_{37} alkenones ($\delta^{13}C_{37}$). C_{37} alkenones are long chain methyl ketones produced by a restricted group of haptophyte algae [*Marlowe et al.,* 1990] and have been used in several studies to reconstruct levels of atmospheric carbon dioxide over time [*Jasper et al.,* 1994; *Pagani et al.,* 2005; *Seki et al.,* 2010]. Haptophyte biomass $\delta^{13}C$ values can be determined by correcting $\delta^{13}C_{37}$ for the biosynthetic offset of 4 ‰ [*Popp et al.,* 1998b]; ε_p values are then determined by reconstructing the carbon isotopic composition of dissolved CO_2 ($\delta^{13}C_{[CO2(aq)]}$). Shallow dwelling

foraminifera have been used previously to determine the DIC $\delta^{13}C$ value used for alkenone paleobarometry. However, the low number of individuals available for analysis here results in a record with a low signal to noise ratio. We therefore estimate surface water DIC $\delta^{13}C$ using fine fraction $\delta^{13}C_{carb}$, with an isotopic offset of +2 ‰ calculated from the mean difference between *G. trilobus* $\delta^{13}C$ and $\delta^{13}C_{carb}$ over CM6. Using this $\delta^{13}C$ record we determine $\delta^{13}C_{[CO2(aq)]}$ with temperature dependant fractionation quantified using Mg/Ca paleothermometry as described above. Calculated ε_p values were converted to $[CO_{2(aq)}]$ using the relationship determined by *Bidigare et al.* [1997] assuming a growth rate (phosphate) dependant b-value of 110.65 for *Emiliania huxleyi*, which is typical for oligotrophic regimes [e.g. *Bidigare et al.,* 1997; *Pagani et al.,* 2010]. Atmospheric pCO_2 is then calculated by applying Henry's law, assuming equilibrium between ocean-atmosphere CO_2 and again using reconstructed SSTs; where necessary, SST was estimated on the basis of linear interpolation in the time domain.

Uncertainty propagation on our alkenone-derived pCO_2 estimates was performed by Monte Carlo modelling (n=25000). Salinity uncertainty was estimated by reconstructing $\delta^{18}O_{sw}$ using paired *G. trilobus* Mg/Ca SST and $\delta^{18}O$ data, assuming all variation in $\delta^{18}O_{sw}$ was due to salinity variations using the sensitivity described in *Maslin et al.* [1995]. This approach produces a maximum uncertainty as most of the variability in $\delta^{18}O_{sw}$ will be due to changing ice volume. Uncertainties of 2 °C and 0.2 ‰ were applied to temperature and $\delta^{13}C_{carb}$, respectively (normal probability function (pdf), 2σ error) and 2.5 mmol and 0.05 psu on salinity and $[PO_4^{3-}]$ respectively (uniform pdf). 2σ errors on $\delta^{13}C_{37}$ were estimated from replicate runs. An 11 % error on the slope of $b=a[PO_4]+c$ was assumed [*Pagani et al.,* 1999].

2.7 Boron based paleobarometry

206 There are two isotopes of boron, ^{10}B and ^{11}B, with natural abundances of ~20 % and ~80
207 %, respectively. Isotope variations are described in delta notation as follows:
208
209 $$\delta^{11}B = \left[\left(\frac{^{11}B/^{10}B_{sample}}{^{11}B/^{10}B_{NIST\ 951}}\right) - 1\right] \times 1000 \quad (3)$$
210
211 where $^{11}B/^{10}B_{NIST951}$ is the $^{11}B/^{10}B$ ratio of NIST SRM 951 boric acid standard ($^{11}B/^{10}B$ =
212 4.04367; *Catanzaro et al.*, [1970]).
213
214 Boron exists as two species in aqueous solutions at typical ocean *p*H: boric acid ($B(OH)_3$)
215 and borate ion ($B(OH)_4^-$). The abundance of these species is *p*H dependent with ~80 % $B(OH)_3$ at
216 typical seawater *p*H. Due to structural differences between the two boron species in seawater
217 there is a pronounced isotopic fractionation between them in seawater, with $B(OH)_3$ being
218 enriched in ^{11}B. In order to maintain a constant $\delta^{11}B$ of seawater, the isotopic composition of each
219 species also varies according to *p*H, for instance, the isotopic composition of $B(OH)_4^-$ is related to
220 *p*H by the following:
221
222
223 $$pH = pK^*_B - \log\left(-\frac{\delta^{11}B_{B_{sw}} - \delta^{11}B_{B(OH)_4^-}}{\delta^{11}B_{B_{sw}} - \alpha_B \cdot \delta^{11}B_{B(OH)_4^-} - ((\alpha_B - 1)\cdot 1000)}\right) \quad (4)$$
224
225 where pK^*_B is the $-1\log_{10}$ of the stoichiometric equilibrium constant for boric acid
226 [*Dickson*, 1990] at the *in situ* temperature, salinity and pressure, $\delta^{11}B_{sw}$ is the isotopic composition
227 of seawater (39.61 ‰; *Foster et al.*, [2010]), $\delta^{11}B_{B(OH)4-}$ is the isotopic composition of borate ion.
228 The isotopic fractionation between the two aqueous species of boron in seawater (α_B) has recently
229 been determined as 1.0272 ± 0.0006 ‰ [*Klochko et al.*, 2006].

On the basis of isotopic measurements of marine carbonates, *Hemming and Hanson* [1992] suggested that the borate ion species is preferentially incorporated into marine carbonate. However, NMR studies [*Klochko et al.,* 2009] have shown that some trigonal BO_3 is also present in $CaCO_3$ which has been used by some to argue that boric acid may also be incorporated into $CaCO_3$. Recent isotopic measurements of benthic foraminifera by MC-ICPMS however confirm that only very minor amounts of boric acid can be incorporated in foraminifera (<1 %; *Rae et al.*, [2011]). Consequently, for epifunal benthic foraminifera measured by MC-ICPMS $\delta^{11}B_{foram} = \delta^{11}B_{B(OH)4-}$, and equation (4) can be used to calculate *p*H.

For the planktic foraminifera *G. trilobus* used here (assuming *G. trilobus* is the same as *G. sacculifer*), it has been shown [*Sanyal et al.*, 2001], using negative ion thermal ionisation mass spectrometry (NTIMS), that there was a strong *p*H dependency of $\delta^{11}B$ but $\delta^{11}B_{foram} \neq \delta^{11}B_{B(OH)4-}$. Here we follow *Foster et al.,* [2012] in order to correct for these "vital effects" and calculate $\delta^{11}B_{B(OH)4}$ from the $\delta^{11}B$ of *G. trilobus* (300-355 µm) by:

$$\delta^{11}B_{B(OH)4-} = \delta^{11}B_{trilobus} \times 0.88 + 1.85 \quad (5)$$

The $\delta^{11}B_{B(OH)4-}$ can then be inserted into equation (4) to calculate *p*H. Since *G. trilobus* is a predominantly mixed layer dweller, we assume that the calculated *p*H is that of surface water.

The stoichometric dissociation constant of boric acid (K^*_B) is temperature, salinity and pressure dependent [*Dickson,* 1990]. These variables do not have a large impact on the calculated *p*H and pCO_2 (e.g. ~10 ppm/ºC; ~2 ppm/psu) and here salinity is assumed to be 35 psu throughout and SST is given by *G. trilobus* Mg/Ca as detailed above.

From equation (4) it can be seen that use of $\delta^{11}B$ in *G. trilobus* to reconstruct *p*H and hence pCO_2 requires an estimate of the isotopic composition of seawater in the past. The oceanic residence time of boron is ~14 Myrs [*Lemarchand et al.,* 2002], and modelling approaches suggest that the seawater boron isotope ratio was lower by up to a few per mil during the Miocene, but the absolute magnitude of the change in seawater $\delta^{11}B$ is largely uncertain [*Lemarchand et al.,* 2002; *Simon et al.,* 2006; *Pearson and Palmer,* 2000; *Paris et al.,* 2010]. Using a modification of the depth profile approach of *Pearson and Palmer* [2000], *Foster et al.,* [2012] calculate $\delta^{11}B_{sw}$ was 37.8 ‰ for the middle Miocene, a value that is in good agreement with the modelling of *Lemarchand et al.* [2002] and the reconstruction of *Pearson and Palmer* [2000]. Given the long residence time of boron in seawater (~14 Myrs; *Lemarchand et al.,* 2002), that value is likely appropriate for our entire record.

To fully reconstruct changes in the ocean carbonate system, two of the six co-varying parameters (*p*H, $[CO_{2(aq)}]$,$[HCO_3^-]$, $[CO_3^{2-}]$, Total Alkalinity and Dissolved Inorganic Carbon) must be known. *Foster et al.,* [2012] calculate surface water alkalinity for the middle Miocene using a modelling approach that closely follows *Tyrrell and Zeebe* [2004] supplemented with new $\delta^{11}B$ measurements of benthic foraminifera to estimate deep water *p*H. By assuming a similar to modern surface to deep alkalinity gradient, *Foster et al.,* [2012] estimate surface water total alkalinity in the middle Miocene to be 1293 ± 200 µmol/kg. The uncertainty in this estimate accounts for uncertainties in the surface-deep gradient, the depth of CCD, and any variations in total alkalinity during the course of our record (see *Foster et al.,* [2012] for details). The uncertainties in pCO_2 we calculate from the boron based-*p*H are dominated by uncertainties in this second carbonate system parameter (± 40 ppm). A quadratic addition of other likely uncertainties, e.g., temperature (± 1 °C) and $\delta^{11}B$ (around ± 20 ppm), gives a total uncertainty of approximately ± 50 ppm. It is important to note that following *Tyrrell and Zeebe* [2004] we also account in all

carbonate system calculations for the effect of changing [Mg] and [Ca] of seawater on the carbonic acid dissociation constants K_1 and K_2 and the solubility product of $CaCO_3$ (K_{sp}), by using the [Ca], [Mg], and Mg/Ca_{sw} taken from the fluid inclusion data of *Horita et al.*, [2002].

The *p*H dependent speciation of boron in seawater also forms the basis for the B/Ca proxy of the carbonate system. It is thought that the incorporation of boron into calcium carbonate can be described by the following equilibria [*Hemming and Hanson*, 1992]:

$$CaCO_3 + B(OH)_4^- \rightarrow Ca(HBO_3) + HCO_3^- + H_2O \quad (6)$$

Following *Zeebe and Wolf-Gladrow* [2001] the following exchange equilibria (K_D) can be defined:

$$K_D = \left(\frac{B/Ca_{solid}}{B(OH)_4^- / HCO_3^-{}_{seawater}} \right) \quad (7)$$

It therefore follows that, since the $B(OH)_4^-$ concentration is *p*H dependent, if K_D can be calibrated and the pH determined (e.g. using boron isotopes), equation (4) can be solved for HCO_3^- providing a second variable of the carbonate system which would allow the whole system to be resolved. However, the K_D for planktic species such as *G. sacculifer* has been shown to be species specific and dependent on test size [*Ni et al.*, 2007] as well as one or several environmental variables (e.g. temperature and/or $[CO_3^{2-}]$; *Yu et al.*, 2007; *Foster*, 2008). A recent culture study has shown that for *G. sacculifer*, temperature had a negligible effect on boron incorporation but K_D was inversely proportional to $[CO_3^{2-}]$, perhaps as a consequence of $[CO_3^{2-}]$ competing with $B(OH)_4$ for the same lattice site [*Allen et al.*, 2011; *Allen et al.*, 2012]. Although *Foster* [2008] presents a core top calibration for *G. sacculifer* (500-600 μm) the relationships between K_D and temperature and $[CO_3^{2-}]$ remain rather poorly defined [*Allen and Honisch*, 2012].

Furthermore, as the evolution of seawater [B] over these timescales is also unknown, we consider that a more quantitative treatment of our B/Ca data would be somewhat premature.

2.8 Carbon cycle modelling

We use the mass balance model of *Kump and Arthur* [1999] to calculate changes in the isotopic composition of inorganic and organic carbon in the ocean/atmosphere system. Changes in the modelled carbon content of the system are driven by changing inputs from weathering and metamorphism/volcanism and outputs from the burial of carbon as carbonate minerals and organic matter. The model accounts for changing ε_p values due to varying pCO_2 and we also include a negative weathering feedback on changing pCO_2 as detailed by *Kump and Arthur* [1999]:

$$F_{wsil}^{t} = F_{wsil}^{0} \cdot [pCO_2^{(t)} / pCO_2^{(0)}] \quad (8)$$

where F_{wsil} is the global silicate weathering flux. In order to simulate Miocene climate we set initial pCO_2 at 330 ppm (derived from our alkenone paleobarometry results) and ran the models for 1 Myrs to reach steady state before starting perturbations. Models were solved numerically using MATLAB (Simulink) with variable step solver ode45.

3. Results and Discussion

Our bulk carbonate oxygen isotope record ($\delta^{18}O_{carb}$) shows the final step ("E3") of the globally recognised increase in $\delta^{18}O$ at the MMCT, and our fine fraction (<63 μm) carbonate carbon isotope record ($\delta^{13}C_{carb}$) shows the distinctive double peak of CM6, confirming that the RIP section faithfully records global changes (Figure 2). Alkenone $\delta^{13}C$ ($\delta^{13}C_{37}$) values are somewhat variable, but display an overall increase across CM6 (Figure 3). The boron-based proxy

data are limited to the older portion of CM6 due to sample availability, but nevertheless also display a consistent increase (Figure 3).

G. trilobus Mg/Ca ratios decrease from 6.6 mmol/mol at the start of the record at 13.799 Ma, to 3.86 mmol/mol by 13.021 Ma (Table 1). For much of the early part of the record only the di-unsaturated alkenone is present suggesting sea surface temperatures (SSTs) exceeded 29 °C (Table 1; *Müller et al.,* 1998); this could reflect enhanced degradation of the tri-unsaturated alkenone, but such differential degradation, even under highly oxidising conditions, appears to increase $U_{37}^{K'}$ by only ~0.1 (equivalent to <0.5 °C; *Huguet et al., 2009).* Moreover, the tri-unsaturated alkenone is present in younger sediments, and $U_{37}^{K'}$ indices reach a minimum value of 0.91 at 13.709 Ma. The high Mg/Ca ratios and $U_{37}^{K'}$ indices suggest high SSTs (> 29 °C) at this point in the Miocene; the SST record determined using our Mg/Ca calibration (Equation (2)) indicates a decrease of about 4 °C following the ice sheet expansion, independent of the value of Mg/Ca_{sw} (Figure 4). We note that even given the large uncertainties surrounding Mg/Ca_{sw} and the response of foraminifera to changing Mg/Ca_{sw}, our Mg/Ca SST estimates are predominantly within uncertainty of our $U_{37}^{K'}$ based estimates (Figures 4 and 5), providing support for the power law approach of *Evans and Müller* [2012].

Our calculated ε_p values are almost identical to published Miocene values [*Pagani et al.*, 1999] determined from similar aged oligotrophic regions, giving us confidence that growth rate effects were minimal in the RIP section, and that the reconstructed pCO_2 is a global, rather than local signature [*Pagani et al.,* 1999] (Figure 5). Our calculated pCO_2 levels of 260 to 350 ppm are slightly higher than those reported previously (~240 ppm) [*Pagani et al.,* 1999; 2005]. This difference is due to our higher sea surface temperature (SST) estimates, which affect air-sea CO_2 equilibria. Post-depositional preservation effects at the deep-sea carbonate-rich sites used by *Pagani et al.* [1999] almost certainly resulted in artificially cool temperature estimates from

oxygen isotope paleothermometry [*Pearson et al.,* 2001], and recently revised Miocene pCO_2 estimates are similar to those observed here [*Pagani et al. 2010*]. The clay-rich lithology at RIP has resulted in excellent preservation of foraminifera enabling more accurate estimates of past SST using Mg/Ca paleothermometry. These differences result in alkenone pCO_2 estimates that are somewhat higher than previously reported by *Pagani et al.,* [1999, 2005] but are still generally low (~300 ppm) and comparable to those measured in other Neogene studies [*Kürschner et al.,* 2008; *Foster et al., 2012*] (Figure 5).

G. trilobus $\delta^{11}B$ values increase across CM6 (Figure 3), which implies an increasing *p*H and decreasing pCO_2 regardless of our choice of seawater $\delta^{11}B$ (Table 2) or second carbonate system parameter. In support of this conclusion, we note that our *G. trilobus* B/Ca record also increases across CM6 (Figure 3), which, in the absence of other complicating factors [*Yu et al.,* 2007; *Foster,* 2008; *Allen et al.,* 2011], also implies an increase in surface water pH and hence decrease in pCO_2 [*Foster,* 2008].

Using a $\delta^{11}B_{sw}$ = 37.8 ‰ [*Foster et al.,* 2012], $\delta^{11}B$-based pH changes from 7.91 ± 0.03 to a maximum of 8.02 ± 0.03. Using this *p*H record, along with a total alkalinity of 1293 ± 200 µmol, yields pCO_2 estimates that drop from 311 ± 55 ppm to a minimum of 230 ± 43 ppm (ΔpCO_2 of ~80 ppm). Importantly, these new pCO_2 estimates using boron isotopes are in very good agreement with our alkenone-based estimates (Figure 4), which provide confidence in the validity of the $\delta^{11}B_{sw}$ and total alkalinity reconstructions of *Foster et al.,* [2012]. Boron isotope compositions of *G. trilobus* from the RIP section are also very similar to middle Miocene aged *G. trilobus* measured by MC-ICPMS by *Foster et al.* [2012] from ODP Site 761 and Site 926.

4. The Miocene Carbon Cycle and Climate

370 Our $\delta^{13}C_{37}$, B/Ca and $\delta^{11}B$ records show positive trends over CM6 (Figure 3); for the
371 former, this yields a decrease in ε_p values. Therefore, regardless of the absolute values or
372 treatment of Mg/Ca_{sw}, the alkenone and boron based-CO_2 proxies all indicate CM6 is associated
373 with a pCO_2 decrease (Figure 4). In order to evaluate potential causes of CM6, we ran a simple
374 ocean carbonate system model [*Kump and Arthur*, 1999] to assess the feasibility of the organic
375 matter burial hypothesis. We inverse model the $\delta^{13}C_{carb}$ increase by assuming it is driven by two
376 discrete pulses of increased organic carbon burial. Under this scenario, the magnitude of the
377 $\delta^{13}C_{carb}$ increase across CM6a and CM6b requires a 70 % and a 50 % increase in organic carbon
378 burial respectively, with each perturbation lasting 41 kyrs (inset; Figure 6a). This results in a 60
379 ppm CO_2 drawdown, which is in agreement with both our alkenone and boron pCO_2 records
380 (Figure 6). This is in contrast to the silicate-weathering hypothesis which would have led to an
381 increase in pCO_2.

382 The model and the records cannot be used to identify a cause of the suggested increase in
383 organic matter burial (i.e., production versus preservation), which prevents a useful feasibility
384 assessment of this modelled scenario. Nevertheless, we note that the magnitude of the organic
385 carbon burial increase required to produce the observed carbon isotope excursion is substantial,
386 and suggesting that other factors may also have been involved. Although our preferred causal
387 mechanism for CM6 involves at least some component of increased organic carbon burial, we
388 cannot rule out other influences on the size and carbon isotopic composition of the ocean-
389 atmosphere reservoir. For example, cooler bottom water temperatures could have facilitated
390 increased sequestration of methane in hydrates, which would represent a reduced flux of ^{13}C-
391 depleted carbon to the atmosphere from the marine realm. Moreover, our model and records do
392 not distinguish between increased organic matter sequestration in marine vs terrestrial realms or,
393 in the case of the former, between burial in continental margins or the deep sea. However, export
394 productivity records from the Atlantic do show a pronounced increase over CM6 [*Diester-Haass*

395 *et al.,* 2009], and there is correlation between the presence of organic-rich sediments and carbon
396 isotope maxima within the Monterey formation [*Flower and Kennett,* 1993a], suggesting that
397 increased burial of organic matter in the marine realm was likely responsible for a major
398 component of the global $\delta^{13}C_{carb}$ excursion.

399 Our records reveal that organic carbon burial during CM6 could have acted as an important
400 positive feedback on ice sheet growth. Global cooling and sea-level fall associated with the initial
401 growth of the ice sheet would have increased meridional thermal gradients and may have
402 increased ocean ventilation [*Flower and Kennett,* 1993a]. This may have led to enhanced
403 biological productivity and CO_2 drawdown as a result of a stronger biological pump, and
404 consequently further cooling [*Flower and Kennett,* 1993a; *Vincent and Berger,* 1985]. Thus, CM6
405 likely illustrates an important positive feedback in the global climate system as opposed to a
406 negative feedback [*Shevenell et al.,* 2008] or a primary forcing mechanism [*Vincent and Berger,*
407 1985] as has been previously suggested.

408 **5. Summary and Conclusions**

409 The largest of the middle Miocene "carbon maxima" events was associated with a pCO_2
410 decrease of 59 ± 63 ppm (from $\delta^{13}C_{37}$) or 82 ± 72ppm (from $\delta^{11}B_{trilobus}$) (e.g. ~ 20 %). Both the
411 magnitude and direction of the isotopic shift and observed pCO_2 change are consistent with an
412 increase in organic carbon burial, perhaps fuelled by increasing oceanic temperature gradients and
413 overturning following the expansion of the Antarctic ice sheet. At this time, we estimate
414 atmospheric pCO_2 was near 300 ppm, somewhat higher than previous alkenone- [*Pagani et al., 1999*] and boron-based [*Pearson and Palmer,* 2000] techniques but in agreement with more
416 recently published long term records [*Kürschner et al.* 2008; *Foster et al.,* 2012]. We attribute
417 these differences to the use of higher sea surface temperatures in the case of the alkenone
418 estimates and more accurate $\delta^{11}B$ determinations. Crucially, our estimates suggest an emerging

419 consensus for Miocene pCO_2 between the alkenone, boron isotope and leaf stomatal approaches
420 (Figure 5). Moreover, these values are only slightly higher than modern pre-industrial values and
421 overlap with the threshold values thought to be required for bipolar glaciation [~280 ppm;
422 *DeConto et al.,* 2008]. Recent modelling studies suggest that changes in North American
423 topography and other boundary conditions in the Miocene prevented glaciation and may have
424 caused a lower pCO_2 threshold for full blown northern hemisphere glaciation to exist during the
425 Miocene [*Foster et al.*, 2010b]. Nonetheless, since sea surface temperatures estimated from both
426 alkenones and *G. trilobus* Mg/Ca ratios at this Mediterranean site indicate temperatures >29 ˚C,
427 our results reaffirm the enigma of a warmer Miocene-world with, at times, less ice than today but
428 only slightly higher levels of atmospheric pCO_2. One potential resolution of these data is that
429 climate sensitivity to pCO_2 is greater than previously thought [*Pagani et al.*, 2010]. The impact of
430 high latitude vegetation on Earth's albedo may have also played an important role in Earth's
431 energy budget in the Miocene [*Knorr et al.,* 2011]. However, further global temperature records
432 are required to solve the Miocene paleoclimate enigma.

433

Acknowledgements. This manuscript is dedicated to the memory of Ben Flower, an inspirational paleoceanographer who will be missed by many. We thank F. J. Hilgen for introducing us to the section, A. A. Mourik for assistance in the field, G. Debono for arranging permissions to work on the section, F. Gill (OGU), J. Becker and J. Green for analytical assistance, P. Pearson for taxonomic assistance and S. Barker for modelling assistance. We also thank Ian D. Bull of the NERC Life Sciences Mass Spectrometry Facility for assistance with alkenone $\delta^{13}C$ determinations. This manuscript was improved by the careful comments of two anonymous reviewers and the editor. This work was supported by NERC and the National Museum Wales in the form of a CASE studentship (M.P.S.B.), NERC grants NE/D008654/1 and NE/D010241/1 (C.H.L. and R.D.P.), a NERC Advanced Fellowship NERC NE/D00876X/2 (G.L.F.) and NIGL award IP/920/1106 (C.H.L. and R.D.P.).

Figure 1: The Ras il-Pellegrin section (35°54.93'N 14°20.06'E). (a) Sampling site, with positions of sampling trenches shown in white (b) View towards the sampling site (marked by white rectangle) across Fomm Ir-Rih Bay (c) Location of sampling site (red star) on the island of Malta (d) Location of Malta in the central Mediterranean Sea.

Figure 2: Multi-proxy records following the middle Miocene Antarctic ice sheet expansion. (a) Bulk carbonate oxygen isotope record from the Ras il-Pellegrin section (this study, orange open triangles and line, *Abels et al.* [2005], gray inverted triangles) (b) Benthic foraminiferal $\delta^{18}O$ record from ODP Site 1146 (gray line; [*Holbourn et al.*, 2005]) (c) Carbonate carbon isotope records from the Ras il-Pellegrin section (fine fraction $\delta^{13}C$ from this study, blue open squares and line, and bulk carbonate $\delta^{13}C$ from *Abels et al.* [2005], gray filled squares) (d) Benthic foraminiferal $\delta^{13}C$ record from ODP Site 1146 (gray line; [*Holbourn et al.*, 2005]). Age models for all records have been retuned following *Mourik et al.*, [2011]. Error bars shown are ±2σ.

Figure 3: Isotope and trace metal records across CM6 from the Ras il-Pellegrin section. (a) Carbonate $\delta^{13}C$ from fine fraction (this study; blue open squares and line) and bulk carbonate (*Abels et al.* [2005]; gray filled squares) (b) alkenone $\delta^{13}C$ (open circles and line) (c) *G. trilobus* $\delta^{11}B$ (filled circles and line) (d) *G. trilobus* B/Ca ratios (black filled squares) and (e) *G. trilobus* Mg/Ca ratios. Error bars shown are ±2σ.

Figure 4: Isotope, temperature and pCO_2 records across CM6 from the Ras il-Pellegrin section (a) Carbonate stable carbon isotopes from fine fraction (this study; blue open squares and line) and bulk carbonate (*Abels et al.* [2005]; gray filled squares), (b) Bulk carbonate oxygen isotopes from this study (orange open triangles and line) and *Abels et al.* [2005] (gray inverted triangles), (c) SST calculated from *G. trilobus* Mg/Ca (filled black circles and line) and from alkenone unsaturation index (open black circles), and (d) atmospheric pCO_2 reconstructions from alkenone isotopes (red open diamonds and solid line with ±2σ error envelopes) and from boron isotopes

(dark blue filled triangles and solid line with propagated analytical uncertainties shown as error bars).

Figure 5: Middle Miocene pCO_2 records. (a) Alkenone $\delta^{13}C$ based ε_p measurements from the Ras il-Pellegrin section (pink open circles with 2σ errors), DSDP sites 588 (filled black triangles and dotted line) and 608 (filled black squares and dashed line) and ODP Site 730 (gray crosses and solid gray line), [*Pagani et al.,* 1999]. The age model of *Pagani et al*., [1999] has been shifted by -130 kyrs to match our age model, based on the positions of CM6 in the two records. (b) Atmospheric pCO_2 records from alkenone $\delta^{13}C$ from Ras il-Pellegrin (this study; red open diamonds and solid line with ±2σ error envelopes) and DSDP Site 588 (dotted line); DSDP Site 608 (dashed line), and ODP Site 730 (solid line) [*Pagani et al.,* 1999], boron isotopes from the Ras il-Pellegrin section (this study; dark blue filled triangles with propagated analytical uncertainties shown as error bars), and ODP Sites 761 (filled black circles) and 926 (open triangles) [*Foster et al.,* 2012], and stomatal indices [*Kürschner et al.,* 2008]. (c) SST record from *G. trilobus* Mg/Ca (black filled circles and line) and alkenone unsaturation index (open circles) from the Ras il-Pellegrin section (this study) and (d) Benthic foraminiferal $\delta^{18}O$ record from ODP Site 1146 (gray line; [*Holbourn et al.,* 2005]).

Figure 6: Carbon dioxide reconstructions and modelling. (a) Boron isotope based atmospheric carbon dioxide reconstruction (dark blue filled triangles with propagated analytical uncertainties shown as error bars) and model CO_2 results (black solid line; see text for description); inset: organic matter burial flux model input. (b) Alkenone $\delta^{13}C$ based pCO_2 reconstruction (red open diamonds and solid line with ±2σ error envelopes) and model pCO_2 results (black solid line) **c** Fine fraction Ras il-Pellegrin $\delta^{13}C$ record (blue open squares and line) and modelled average carbonate $\delta^{13}C$ (black solid line).

References

Abels, H.A., F.J. Hilgen, W. Krijgsman, R.W. Kruk, I. Raffi, E. Turco, and W.J Zachariasse (2005), Long-period orbital control on middle Miocene global cooling: Integrated stratigraphy and astronomical tuning of the Blue Clay Formation on Malta, *Paleoceanography*, *20*, PA4012, doi:10.1029/2004PA001129.

Allen, K., B. Hönisch, S. M. Eggins, J. Yu, H.J. Spero, H. Elderfield. (2011) Controls on boron incorporation in cultured tests of the planktic foraminifer *Orbulina universa*, *Earth Planet. Sci. Lett., 309,* 291-301

Allen, K., and B. Hönisch, (2012), The planktic foraminiferal B/Ca proxy for seawater carbonate chemistry: A critical evaluation, *Earth Planet. Sci. Lett., 345-348*, 203-211, doi:10.1016/j.epsl.2012.06.012

Anand, P., H. Elderfield, and M. H. Conte (2003), Calibration of Mg/Ca thermometry in planktonic foraminifera from a sediment trap time series, *Paleoceanography*, 18(2) doi:10.1029/2002PA000846.

Barker, S., M. Greaves, and H. Elderfield (2003), A study of cleaning procedures used for foraminiferal Mg/Ca paleothermometry, *Geochem. Geophys. Geosyst*., *4*, doi:10.1029/2003GC000559.

Bellanca, A., F Sgarrella, R. Neri, B. Russo, M. Sproviera, G. Bonaduce and D. Rocca (2002), Evolution of the Mediterranean basin during the late Langhian early Serravallian: An integrated paleoceanographic approach,), *Riv. Ital. Paleontol. Stratigr., 108*, 223-239.

Bidigare, R.R., A. Fluegge, K.H. Freeman, K.L. Hanson, J.M. Hayes, D. Hollander, J.P. Jasper, L.L. King, E.A. Laws, J. Milder, F.J. Millero, R. Pancost, B.N. Popp, P.A. Steinberg, and S.G. Wakeham (1997), Consistent fractionation of C-13 in nature and in the laboratory: Growth-rate effects in some haptophyte algae, *Global Biogeochem. Cycles*, 11, 279-292.

Billups, K., and D. P. Schrag (2002), Paleotemperatures and ice volume of the past 27 Myr revisited with paired Mg/Ca and $^{18}O/^{16}O$ measurements on benthic foraminifera, *Paleoceanography*, *17*, doi:10.1029/2000PA000567.

Bonaduce, G., and D. Barra (2002), The ostracods in the paleoenvironmental interpretation of the late Langhian-early Serravallian Ras il-Pellegrin section (Malta), *Riv. Ital. Paleontol. Stratigr., 108,* 211-222.

Catanzaro, E.J., C.E. Champion, E.L. Garner, G. Marinenko, K.M. Sappenfield, and W.R. Shields, (1970), *Boric assay; isotopic and assay standard reference materials.* Institute for Materials Research, National Bureau of Standards, Washington, D.C.

Coggon, R. M., D. A. H. Teagle, C. E. Smith-Duque, J. C. Alt, and M. J. Cooper (2010), Reconstructing Past Seawater Mg/Ca and Sr/Ca from Mid-Ocean Ridge Flank Calcium Carbonate Veins, *Science, 327*(5969), 1114-1117.

Dart, C.J., D.W.J. Bosence, and K.R. McClay (1993), Stratigraphy and Structure of the Maltese Graben System, *J. Geol. Soc*.,150, 1153-1166.

DeConto, R.M., D. Pollard, P.A. Wilson, H. Palike, C.H. Lear, and M. Pagani (2008), Thresholds for Cenozoic bipolar glaciation, *Nature*, 455, 652-657.

Delaney, M., A. W. H. Bé, and E. A. Boyle (1985), Li, Sr, Mg, and Na in foraminiferal calcite shells from laboratory culture, sediment traps, and sediment cores, *Geochim. Cosmochim. Acta*, *49*(6), 1327–1341.

Dickson, A., (1990). Thermodynamics of the dissociation of boric acid in synthetic seawater from 273.15 to 318.15K. *Deep-Sea Res. A. Oceanogr. Rs Pap. 37*, 755-766.

Dickson, J. A. D. (2002), Fossil echinoderms as monitor of the Mg/Ca ratio of phanerozoic oceans, *Science*, *298*(5596), 1222-1224.

Dickson, J. A. D. (2004), Echinoderm skeletal preservation: Calcite-aragonite seas and the Mg/Ca ratio of phanerozoic oceans, *J. Sediment Res.*, *74*(3), 355-365.

Diester-Haass, L., K. Billups, D.R. Gröcke, L. François, V. Lefebvre, and K.C. Emeis (2009), Mid-Miocene paleoproductivity in the Atlantic Ocean and implications for the global carbon cycle, *Paleoceanography*, *24*, PA1209, doi:1029/2008PA001605.

Evans, D., and W. Müller (2012), Deep time foraminifera Mg/Ca palaeothermometry: Nonlinear correction for secular change in seawater Mg/Ca, *Paleoceanography*, *27*, PA4205, doi:10.1029/2012PA002315.

Fantle, M.S., DePaolo, D.J., 2006. Sr isotopes and pore fluid chemistry in carbonate sediment of the Ontong Java Plateau: calcite recrystallization rates and evidence for a rapid rise in seawater Mg over the last 10 million years. *Geochim. Cosmochim. Acta, 70*, 3883–3904.

Fantle, M.S., DePaolo, D.J., 2005. Variations in the marine Ca cycle over the past 20 million years. *Earth Planet. Sci. Lett*. *237*, 102–117.

Flower, B.P., and J.P. Kennett (1993a), Relations between Monterey Formation Deposition and Middle Miocene Global Cooling - Naples-Beach Section, California, *Geology*, *21*, 877-880.

Flower, B.P., and J.P. Kennett (1993b), Middle Miocene ocean-climate transition: high resolution oxygen and carbon isotopic records from DSDP Site 588A, southwest Pacific, *Paleoceanography*, *8*, 811-843.

Flower, B.P., and J.P. Kennett (1995), Middle Miocene deep water paleoceanography in the southwest Pacific: Relations with East Antarctic ice sheet development, *Paleoceanography*, *10*, 1095-1112.

Foster, G.L. (2008), Seawater pH, pCO_2 and (CO_3^{2-}) variations in the Caribbean Sea over the last 130 kyr: A boron isotope and B/Ca study of planktic foraminifera, *Earth Planet. Sci. Lett*., *271*, 254-266.

Foster, G.L., D.J Lunt and R.R. Parrish, (2010), Mountain uplift and the glaciation of North America – a sensitivity study. *Climate of the Past, 6*,(5), 707-717. doi:10.5194/cp-6-707-2010

569 Foster, G.L., C.H., Lear, and J.W.B. Rae, (2012), The evolution of pCO_2, ice volume and climate
570 during the middle Miocene. *Earth Planet. Sci. Lett.*, *341-344*, 243-254,
571 doi:10.1016/j.epsl.2012.06.007.

572 Handley, L., P.N. Pearson, I.K. McMillan, and R.D. Pancost (2008), Large terrestrial and marine
573 carbon and hydrogen isotope excursions in a new Paleocene/Eocene boundary section
574 from Tanzania, *Earth Planet. Sci. Lett*, 275, 17-25.

575 Hardie, L. A. (1996), Secular variation in seawater chemistry: An explanation for the coupled
576 secular variation in the mineralogies of marine limestones and potash evaporites over the
577 past 600 my, *Geology*, *24*(3), 279-283.

578 Hasiuk, F. J. and K. C. Lohmann (2010). Application of calcite Mg partitioning functions to the
579 reconstruction of paleocean Mg/Ca. *Geochim. Cosmochim. Acta 74*(23), 6751-6763.

580 Hemleben, C., M. Spindler and O.R. Anderson (1989) *Modern Planktonic Foraminifera.*
581 Springer-Verlag, New York.

582 Holbourn, A., W. Kuhnt, M. Schulz, and H. Erlenkeuser (2005), Impacts of orbital forcing and
583 atmospheric carbon dioxide on Miocene ice-sheet expansion, *Nature*, *438*, 483-487.

584 Holbourn, A., W. Kuhnt, M. Schulz, and J. Flores (2007), Orbitally-paced climate evolution
585 during the middle Miocene "Monterey" carbon-isotope excursion, *Earth Planet. Sci.*
586 *Lett*., *261*, 534-550.

587 Hollander, D.J., and J.A. Mckenzie (1991), CO_2 Control on Carbon-Isotope Fractionation During
588 Aqueous Photosynthesis - a Paleo-pCO_2 Barometer, *Geology*, *19*, 929-932.

589 Hönisch, B. J. Bijma, A D. Russell, H J. Spero, M. R. Palmer, R. E. Zeebe, and A. Eisenhauer
590 (2003) The influence of symbiont photosynthesis on the boron isotopic composition of
591 foraminifera shells. *Marine Micropaleontology 49*, 87-96.

592 Hönisch, B. and G.N. Hemming, (2004).Ground-truthing the boron isotope-paleo-pH proxy in
593 planktonic foraminifera shells: Partial dissolution and shell size effects.
594 *Paleoceanography 19*, PA4010, doi:10.1029/2004PA001026.

595 Horita, J., H. Zimmermann and H.D. Holland (2002), Chemical evolution of seawater during the
596 Phanerozoic: Implications from the record of marine evaporites, *Geochim. et Cosmochim.*
597 *Acta*, *66*, 3733-3756.

598 Huguet, C., J-H. Kim, G. J. de Lange, J. S. Sinninghe Damste and S. Schouten (2009), Effects of
599 long term oxic degradation on the $U_{37}^{K'}$, TEX_{86} and BIT organic proxies: *Org. Geochem.*,
600 *40*, 1188-1194, doi:10.1016/j.orggeochem.2009.09.003.

601 Jasper, J.P., J.M. Hayes, A.C. Mix, and F.G. Prahl (1994), Photosynthetic fractionation of 13C and
602 concentrations of dissolved CO2 in the central equatorial Pacific during the last 255,000
603 years, *Paleoceanography*, *9*, 781-798.

604 Knorr, G., M. Butzin, M., A Micheels and G.Lohmann (2011), A warm Miocene climate at low
605 atmospheric CO_2 levels, *Geophys. Res. Lett. 38*, L20701, doi:10.1029/2011GL048873.

606 Kump, L.R., and M.A. Arthur (1999), Interpreting carbon-isotope excursions: carbonates and
607 organic matter, *Chem. Geol*., 161, 181-198.

608 Klochko, K., A. J. Kaufman, W. S. Yao, R. H. Byrne, and J. A. Tossell (2006), Experimental
609 measurement of boron isotope fractionation in seawater, *Earth Planet. Sci. Lett.*, *248*(1-
610 2), 276-285.

611 Klochko, K., Cody, G. D., Tossell, J. A., Dera, P. & Kaufman, A. J. (2009) Re-evaluating boron
612 speciation in biogenic calcite and aragonite using ^{11}B MAS NMR. *Geochm. et*
613 *Cosmochim. Acta, 73*, 1890-1900, doi:10.1016/j.gca.2009.01.002.

614 Kürschner, W.M., Z. Kvaček, and D.L. Dilcher (2008), The impact of Miocene atmospheric
615 carbon dioxide fluctuations on climate and the evolution of terrestrial ecosystems, *Proc.*
616 *Natl. Acad. Sci. U.S.A.*, 105, 449-453.

617 Laws, E.A, B.N . Popp, R.R. Bidigare, M.C. Kennicutt, S.A. Macko, (1995) Dependence of
618 phytoplankton carbon isotope composition on growth rate and $[CO_2]_{aq}$: Theoretical
619 considerations and experimental results, *Geochm. et Cosmochim. Acta, 59*, 1131-1138

620 Lear, C. H., et al. (2000), Cenozoic deep-sea temperatures and global ice volumes from Mg/Ca in
621 benthic foraminiferal calcite, *Science*, *287*, 269-272.

622 Lear, C.H., Y. Rosenthal, H.K. Coxall, and P.A. Wilson, (2004), Late Eocene to early Miocene ice
623 sheet dynamics and the global carbon cycle, *Paleoceanography*, 19, PA4015,
624 doi:10.1029/2004PA001039.

625 Lemarchand, D., J. Gaillardet, E. Lewin, and C.J. Allègre (2002), Boron isotope systematics in
626 large rivers: Implications for the marine boron budget and paleo-pH reconstruction over
627 the Cenozoic, *Chem. Geol*., 190, 123-140.

628 Locarnini, R. A., A. V. Mishonov, J. I. Antonov, T. P. Boyer, and H. E. Garcia, (2010). World
629 Ocean Atlas 2009, Volume 1: Temperature. S. Levitus, Ed. NOAA Atlas NESDIS 68,
630 U.S. Government Printing Office, Washington, D.C.

631 Lowenstein, T. K., M. N. Timofeeff, S. T. Brennan, L. A. Hardie, and R. V. Demicco (2001),
632 Oscillations in Phanerozoic seawater chemistry: Evidence from fluid inclusions, *Science*,
633 *294*(5544), 1086-1088.

634 Marlowe, I.T., S.C. Brassell, G. Eglinton, and J.C. Green (1990), Long-chain alkenones and alkyl
635 alkenoates and the fossil coccolith record of marine sediments, *Chem. Geol*., 88, 349-375.

636 Maslin, M. A., N.J. Shackleton, and U. Pflaumann (1995), Surface-Water Temperature, Salinity,
637 and Density Changes in the Northeast Atlantic during the Last 45,000 Years - Heinrich
638 Events, Deep-Water Formation, and Climatic Rebounds, *Paleoceanography* 10, 527-544.

639 Miller, K.G., J.D. Wright, and R.G. Fairbanks (1991), Unlocking the ice house: Oligocene-
640 Miocene oxygen isotopes, eustacy and margin erosion, *J. Geophys. Res*., 96, 6829-6848.

641 Mourik, A.A., H.A. Abels, F.J. Hilgen, A. Di Stefano, and W.J. Zachariasse (2011), Improved
642 astronomical age constraints for the Middle Miocene Climate Transition based on high-
643 resolution stable isotope records from the central Mediterranean Maltese Islands,
644 *Paleoceanography*, 26, PA1210, doi: 10.1029/2010PA001981.

645 Müller, P.J., G. Kirst, G. Ruhland, I. von Storch, and A. Rosell-Mele (1998), A calibration of the
646 alkenone paleotemperature index U-37(K') based on core-tops from the eastern South
647 Atlantic and the global ocean (60 degrees N-60 degrees S), *Geochim. Cosmochim. Acta, 62*, 1757-1772.

649 Ni, Y.Y., G.L. Foster, T.R. Bailey, T. Elliott, D.N. Schmidt, P. Pearson, B. Haley, and C. Coath
650 (2007), A core top assessment of proxies for the ocean carbonate system in surface-
651 dwelling foraminifers, *Paleoceanography, 3*, doi:PA3212/000248900900001.

652 Pagani, M., M.A. Arthur, and K.H. Freeman (1999), Miocene evolution of atmospheric carbon
653 dioxide, *Paleoceanography*, 14, 273-292.

654 Pagani, M., J.C. Zachos, K.H. Freeman, B. Tipple, and S. Bohaty (2005), Marked decline in
655 atmospheric carbon dioxide concentrations during the Paleogene, *Science*, 309, 600-603.

656 Pagani, M., K. Caldeira, R. Berner, and D.J. Beerling (2009), The role of terrestrial plants in
657 limiting atmospheric CO_2 decline over the past 24 million years, *Nature*, *460*, 85-89.

658 Pagani, M., Z. Liu, J. LaRiviere and A. C. Ravelo (2010) High Earth-system climate sensitivity
659 determined from Pliocene carbon dioxide concentrations, *Nature Geosciences, 3*, 29-30
660 doi:10.1038/NGEO27

661 Paris, G., J. Gaillardet and P Louvat (2010) Geological evolution of seawater boron isotopic
662 composition recorded in evaporate, *Geology, 38*, 1035-1038, doi:10.1130/G31321.11

663 Pearson, P.N., P.W. Ditchfield, J. Singano, K.G. Harcourt-Brown, C.J. Nicholas, R.K. Olsson,
664 N.J. Shackleton, and M.A. Hall (2001), Warm tropical sea surface temperatures in the
665 Late Cretaceous and Eocene epochs, *Nature*, 413, 481-487.

666 Pearson, P.N., and M.R. Palmer (2000), Atmospheric carbon dioxide concentrations over the past
667 60 million years, *Nature*, 406, 695-699.

668 Popp, B.N., F. Kenig, S.G. Wakeham, E.A. Laws, and R.R. Bidigare (1998a), Does growth rate
669 affect ketone unsaturation and intracellular carbon isotopic variability in Emiliania
670 huxleyi?, *Paleoceanography*, 13, 35-41.

671 Popp, B.N., E.A. Laws, R.R. Bidigare, J.E. Dore, K.L. Hanson, and S.G. Wakeham (1998b),
672 Effect of phytoplankton cell geometry on carbon isotopic fractionation, *Geochim.*
673 *Cosmochim. Acta*, 62, 69-77.

674 Rae., J.W.B., G.L. Foster, D.N. Schmidt and T. Elliot, (2011), Boron isotopes and B/Ca in benthic
675 foraminifera: proxies for the deep ocean carbonate system. *Earth and Planet. Sci. Lett.*,
676 *302*, 403-413.

677 Sanyal, A., J. Bijma, H. Spero, and D. W. Lea (2001), Empirical relationship between pH and
678 boron isotopic composition of *Globigerinoides sacculifer*: Implications for the boron
679 isotope paleo-pH proxy, *Paleoceanography*, 16, 515–519.

680 Seki, O., G. L. Foster, D.N. Schmidt, A. Mackensen, K.K. Kawamure, and R.D. Pancost (2010),
681 Alkenone and boron based Plio-Pleistocene pCO2 records, *Earth Planet. Sci. Lett.*, *292*,
682 201-211.

683 Shevenell, A.E., J.P. Kennett, and D.W. Lea (2008), Middle Miocene ice sheet dynamics, deep-
684 sea temperatures, and carbon cycling: A Southern Ocean perspective, *Geochem.*
685 *Geophys. Geosyst.*, *9*, Q02006, doi:10.1029/2007GC001736.

686 Simon, L., C. Lécuyer, C. Maréchal, and N. Coltice (2006), Modelling the geochemical cycle of
687 boron: Implications for the long-term delta B-11 evolution of seawater and oceanic crust,
688 *Chem. Geol*., 225, 61-76.

689 Tian, J., A. Shevenell, P. Wang, Q. Zhao , Q. Li, and X. Cheng, (2009). Reorganization of Pacific
690 Deep Waters linked to middle Miocene Antarctic cryosphere expansion: A perspective from
691 the South China Sea. *Palaeogeog., Palaeoclimatol., Palaeoecol., 284*(3-4), 375-382, doi:
692 10.1016/j.palaeo.2009.10.019.

693 Tyrrell, T., and R. E. Zeebe (2004), History of carbonate ion concentration over the last 100
694 million years, *Geochim. Cosmochim. Acta.*, *68*(17), 3521-3530.

695 Vincent, E., and W.H. Berger (1985), Carbon dioxide and polar cooling in the Miocene: the
696 Monterey hypothesis in *The carbon cycle and atmospheric CO2: natural variations*
697 *Archean to present. Chapman conference papers*, 1984, 455-468.

698 Wilkinson, B.H., and T.J. Algeo (1989), Sedimentary carbonate record of calcium-magnesium
699 cycling. *Am. J. Sci*., 289, 1158–1194.

700 Woodruff, F., and S. Savin (1991), Mid-Miocene isotope stratigraphy in the deep sea: high
701 resolution correlations, paleoclimatic cycles, and sediment preservation,
702 *Paleoceanography*, 6, 755-806.

703 Yu, J. M., H. Elderfield, and B. Honisch (2007), B/Ca in planktonic foraminifera as a proxy for
704 surface seawater pH, Paleoceanography, 22(2).

705 Zachos, J., M. Pagani, L. Sloan, E. Thomas, and K. Billups (2001), Trends, rhythms, and
706 aberrations in global climate 65 Ma to present, *Science*, 292, 686-693.

707 Zeebe, R. E., Wolf-Gladrow, D. A., Bijma, J. & Hönisch, B. (2003) Vital effects in foraminifera
708 do not compromise the use of $\delta^{11}B$ as a paleo-pH indicator: evidence from modeling.
709 *Paleoceanography 18*, 1043.

710

711

712 **Table 1:** $U_{37}^{K'}$ temperatures and planktic foraminiferal *(G. trilobus)* Mg/Ca and Mg/Ca-
713 temperatures from the Blue Clay Formation at Ras il-Pellegrin, Malta.
714

Height in Section	Age [*Mourik et al.*, 2011]	U^{K}_{37}'	SST[a] [*Müller et al.*, 1998]	*G. trilobus* Mg/Ca Ratio	SST
(m)	(Ma)		(°C)	(mmol/mol)	(°C)
0.00	13.799	1	29.0*	6.56	33.5
0.35	13.792	1	29.0*	5.74	32.0
0.70	13.786	1	29.0*	5.03	30.6
1.05	13.779	1	29.0*	5.17	30.9
1.75	13.766	1	29.0*	5.43	31.4
2.45	13.753	1	29.0*	4.22	28.6
2.80	13.747			4.79	30.0
3.15	13.741	1	29.0*	5.00	30.5
3.50	13.736	1	29.0*	4.13	28.4
3.85	13.731	1	29.0*	4.78	30.0
4.90	13.709	0.909	26.2	4.97	30.4
5.25	13.704	0.985	28.5	4.38	29.0
5.60	13.698	0.987	28.6	4.72	29.9
6.65	13.679	1	29.0*	3.71	27.2
7.35	13.665	0.981	28.4	4.29	28.8
7.70	13.658	1	29.0*	4.39	29.0
8.05	13.651	1	29.0*	4.36	29.0
8.40	13.644	1	29.0*		
9.10	13.628	0.997	28.9	4.36	29.0
9.45	13.620	1	29.0*	4.09	28.3
10.15	13.602	0.979	28.3		
10.50	13.592			4.52	29.4
11.20	13.571	0.960	27.8		
18.20	13.408	0.967	28.0		
22.75	13.301	0.964	27.9	3.92	27.8
33.95	13.021	0.978	28.3	3.86	27.6
43.05	12.811	0.987	28.6		

715

716 [a]Note that the $U_{37}^{K'}$ paleothermometer cannot be used for temperatures greater than 29 °C, so
717 temperatures marked with a * should be considered minimum estimates.
718

719 **Table 2:** Sea surface pH and atmospheric pCO_2 calculated from the maximum and minimum
720 $\delta^{11}B_{foram}$ values from our record for a range of assumed $\delta^{11}B_{SW}$ calculated assuming
721 TA=1300.
722

Assumed Seawater $\delta^{11}B$ (‰)	Calculated surface pH for $\delta^{11}B_{foram}$= 16.66	Calculated surface pH for $\delta^{11}B_{foram}$= 15.86	calculated pCO_2 for $\delta^{11}B_{foram}$= 16.66	calculated pCO_2 for $\delta^{11}B_{foram}$= 15.86	Calculated CO_2 change between maximum and minimum $\delta^{11}B_{foram}$
36	8.167	8.071	148	196	48
37	8.090	7.987	188	252	64
38	8.005	7.895	242	329	87
39	7.910	7.788	318	444	126
40	7.801	7.660	430	627	197

723
724

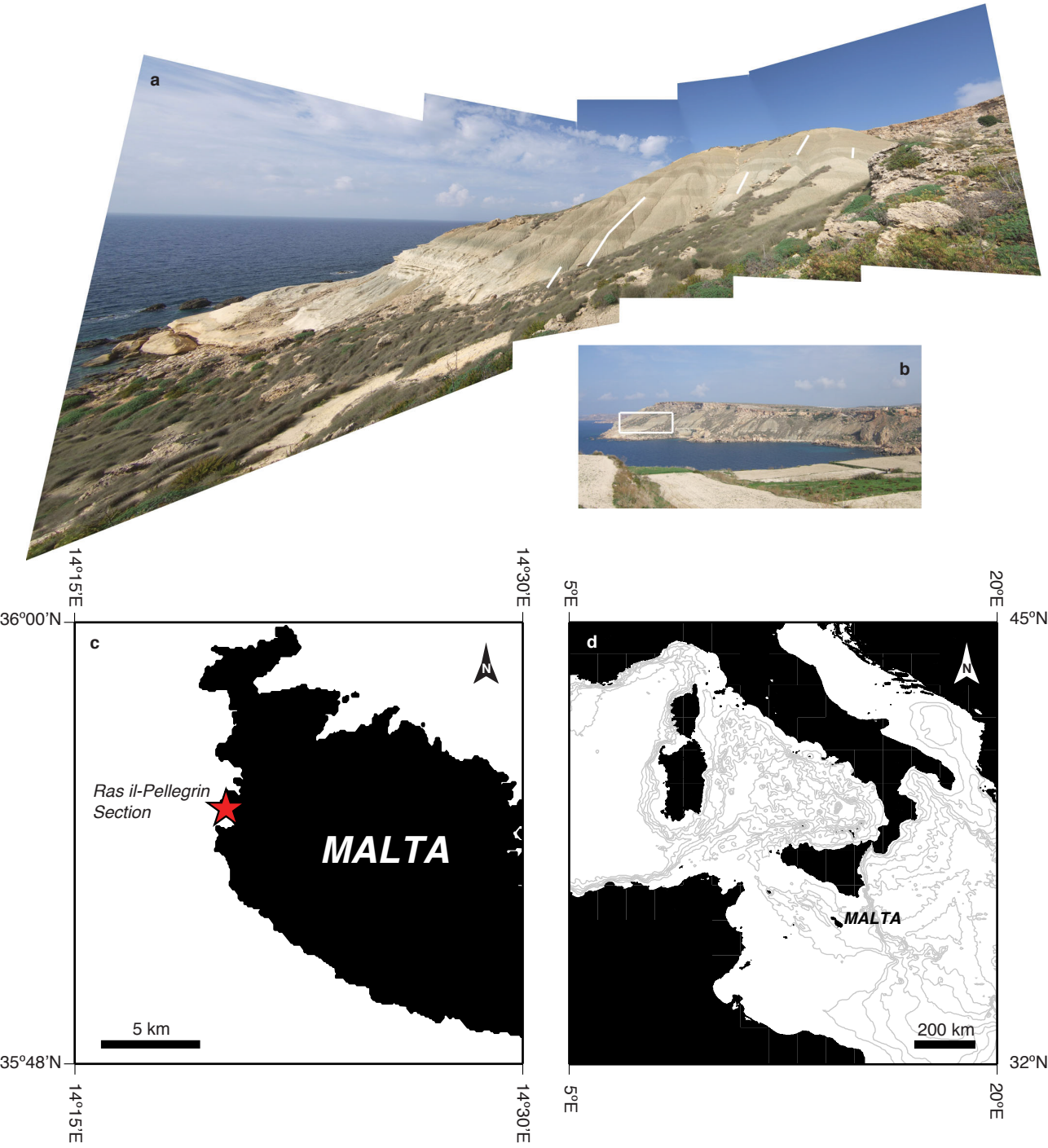

Figure 1: The Ras il-Pellegrin section (35°54.93'N 14°20.06'E). (a) Sampling site, with positions of sampling trenches shown in white (b) View towards the sampling site (marked by white rectangle) across Fomm Ir-Rih Bay (c) Location of sampling site (red star) on the island of Malta (d) Location of Malta in the central Mediterranean Sea.

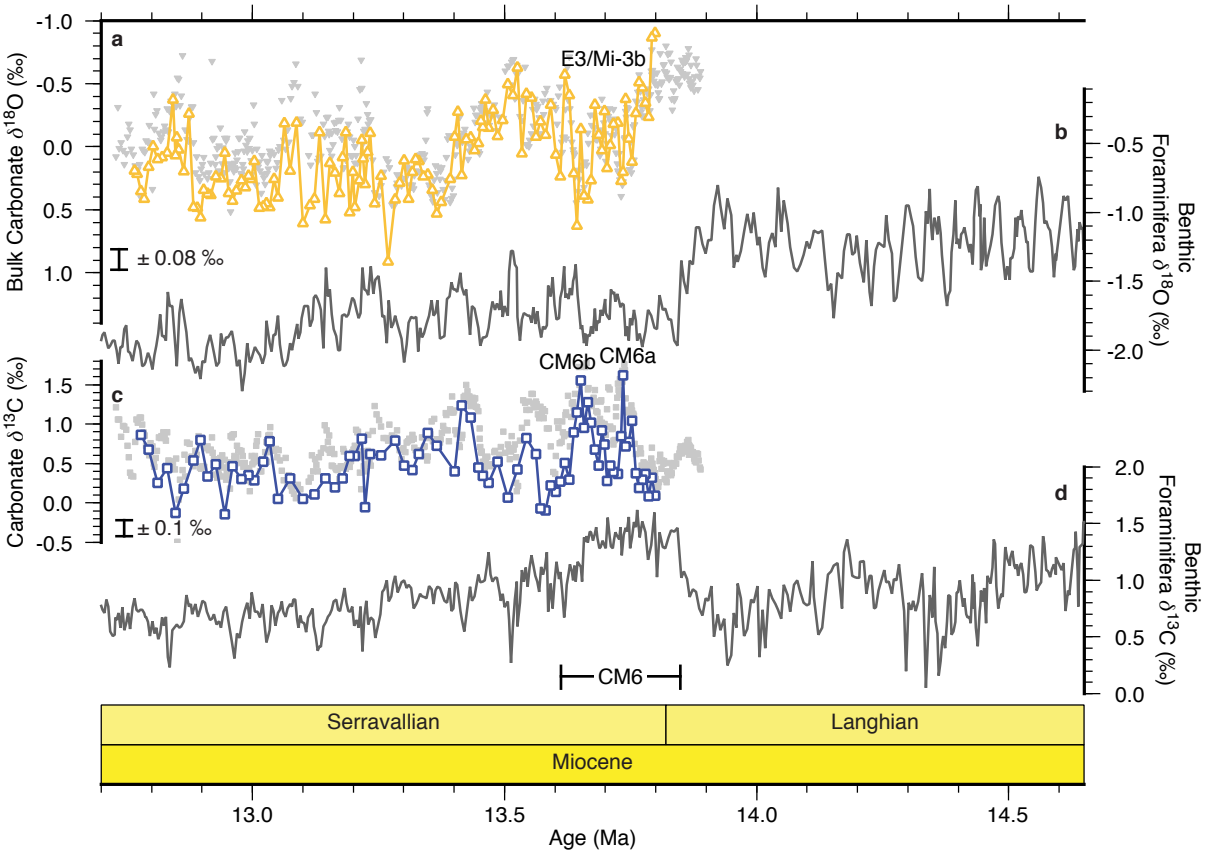

Figure 2: Multi-proxy records following the middle Miocene Antarctic ice sheet expansion. (a) Bulk carbonate oxygen isotope record from the Ras il-Pellegrin section (this study, orange open triangles and line, *Abels et al.* [2005], gray inverted triangles) (b) Benthic foraminiferal $\delta^{18}O$ record from ODP Site 1146 (gray line; [*Holbourn et al.,* 2005]) (c) Carbonate carbon isotope records from the Ras il-Pellegrin section (fine fraction $\delta^{13}C$ from this study, blue open squares and line, and bulk carbonate $\delta^{13}C$ from *Abels et al.* [2005], gray filled squares) (d) Benthic foraminiferal $\delta^{13}C$ record from ODP Site 1146 (gray line; [*Holbourn et al.*, 2005]). Age models for all records have been retuned following *Mourik et al.,* [2011]. Error bars shown are ±2σ.

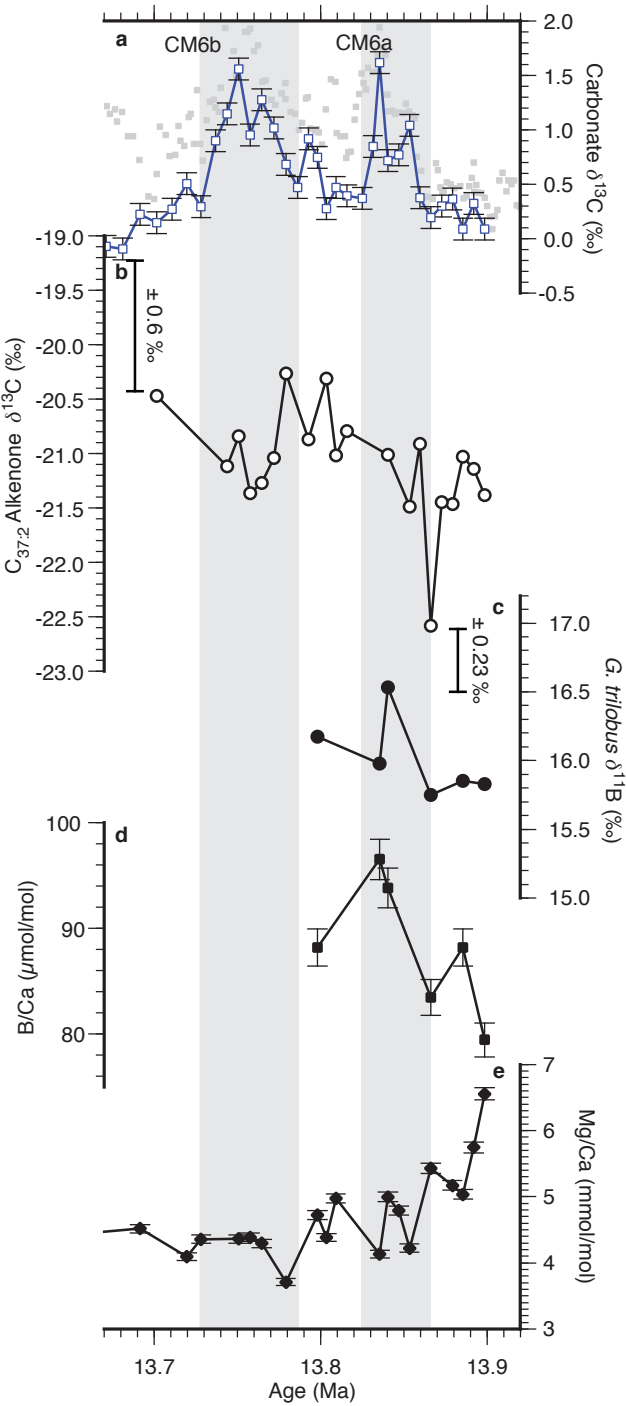

Figure 3: Isotope and trace metal records across CM6 from the Ras il-Pellegrin section. (a) Carbonate $\delta^{13}C$ from fine fraction (this study; blue open squares and line) and bulk carbonate (*Abels et al.* [2005]; gray filled squares) (b) alkenone $\delta^{13}C$ (open circles and line) (c) *G. trilobus* $\delta^{11}B$ (filled circles and line) (d) *G. trilobus* B/Ca ratios (black filled squares) and (e) *G. trilobus* Mg/Ca ratios. Error bars shown are ±2σ.

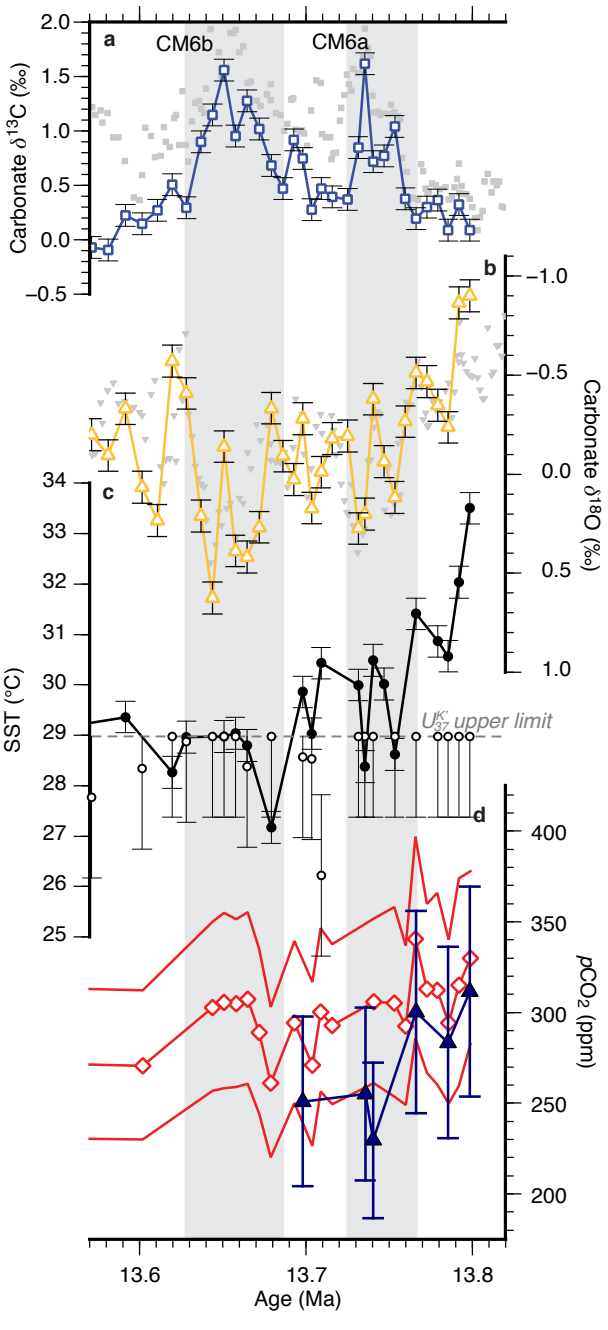

Figure 4: Isotope, temperature and pCO_2 records across CM6 from the Ras il-Pellegrin section (a) Carbonate stable carbon isotopes from fine fraction (this study; blue open squares and line) and bulk carbonate (*Abels et al.* [2005]; gray filled squares), (b) Bulk carbonate oxygen isotopes from this study (orange open triangles and line) and *Abels et al.* [2005] (gray inverted triangles), (c) SST calculated from *G. trilobus* Mg/Ca (filled black circles and line) and from alkenone unsaturation index (open black circles), and (d) atmospheric pCO_2 reconstructions from alkenone isotopes (red open diamonds and solid line with ±2σ error envelopes) and from boron isotopes (dark blue filled triangles and solid line with propagated analytical uncertainties shown as error bars).

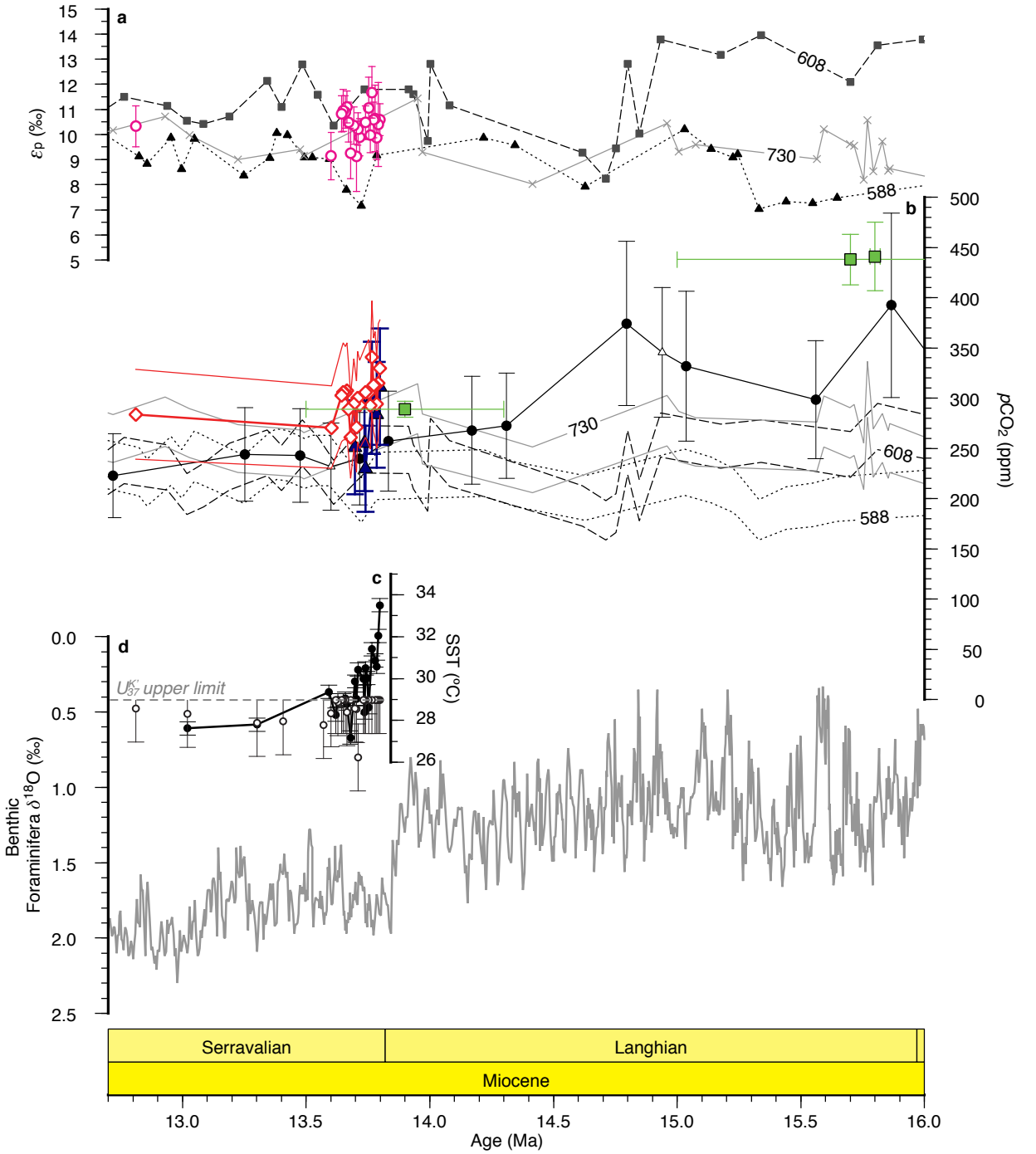

Figure 5: Middle Miocene pCO_2 records. (a) Alkenone $\delta^{13}C$ based ε_p measurements from the Ras il-Pellegrin section (pink open circles with 2σ errors), DSDP sites 588 (filled black triangles and dotted line) and 608 (filled black squares and dashed line) and ODP Site 730 (gray crosses and solid gray line), [*Pagani et al.*, 1999]. The age model of *Pagani et al.*, [1999] has been shifted by -130 kyrs to match our age model, based on the positions of CM6 in the two records. (b) Atmospheric pCO_2 records from alkenone $\delta^{13}C$ from Ras il-Pellegrin (this study; red open diamonds and solid line with ±2σ error envelopes) and DSDP Site 588 (dotted line); DSDP Site 608 (dashed line), and ODP Site 730 (solid line) [*Pagani et al.*, 1999], boron isotopes from the Ras il-Pellegrin section (this study; dark blue filled triangles with propagated analytical uncertainties shown as error bars), and ODP Sites 761 (filled black circles) and 926 (open triangles) [*Foster et al.*, 2012], and stomatal indices [*Kürschner et al.*, 2008]. (c) SST record from *G. trilobus* Mg/Ca (black filled circles and line) and alkenone unsaturation index (open circles) from the Ras il-Pellegrin section (this study) and (d) Benthic foraminiferal $\delta^{18}O$ record from ODP Site 1146 (gray line; [*Holbourn et al.*, 2005]).

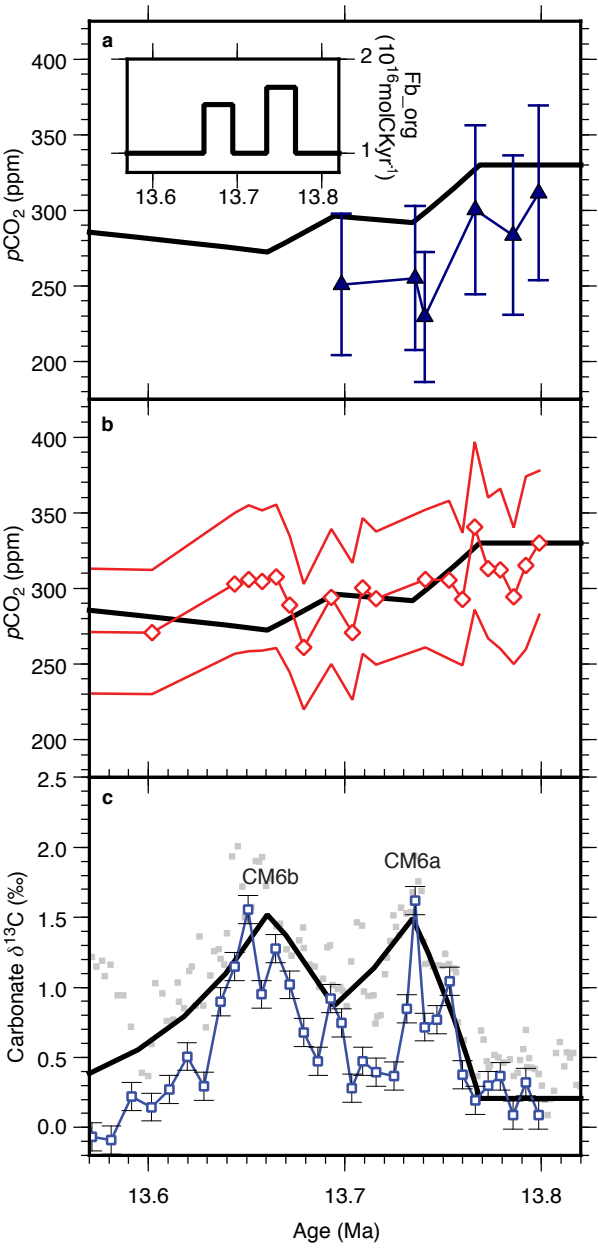

Figure 6: Carbon dioxide reconstructions and modelling. (a) Boron isotope based atmospheric carbon dioxide reconstruction (dark blue filled triangles with propagated analytical uncertainties shown as error bars) and model CO_2 results (black solid line; see text for description); inset: organic matter burial flux model input. (b) Alkenone $\delta^{13}C$ based pCO_2 reconstruction (red open diamonds and solid line with $\pm 2\sigma$ error envelopes) and model pCO_2 results (black solid line) (c) Fine fraction Ras il-Pellegrin $\delta^{13}C$ record (blue open squares and line) and modelled average carbonate $\delta^{13}C$ (black solid line).